von Karman Institute for Fluid Dynamics

Lecture Series 2025-01

MEASUREMENT, MODELLING AND SIMULATIONS TECHNIQUES FOR NOVEL AIRCRAFT ARCHITECTURES

November 4-6, 2024

ON THE ART OF COMBINING EXPERIMENTAL AND NUMERICAL TECHNIQUES TO ASSESS AEROACOUSTIC INSTALLATION EFFECTS

D. Ragni[1]; F. De Prenter[1]; F. Avallone[1]; F. Monteiro[1]; H. Dekker[1,2]; A. Zarri[3]
[1]TU Delft, the Netherlands
[2]NLR, the Netherlands
[3]von Karman Institute for Fluid Dynamics, Belgium

On the art of combining experimental and numerical techniques to assess aeroacoustic installation effects

D. Ragni, F. De Prenter, F. Avallone, F. Monteiro, H. Dekker, A. Zarri
ENODISE Lecture Series, von Karman Institute for Fluid Dynamics, 1640 Rhode-St-Genèse, Belgium

The lecture notes "on the art of combining experimental and numerical techniques to assess aeroacoustic installation effects" describe how combining different experimental and numerical techniques allows us to understand better the phenomena related to installation effects in interacting components. Two test cases are used as examples in the lecture. The first focuses on the aerodynamic and acoustic interference effects of an array of three co-rotating and adjacent propellers, while the second one treats a "propeller over the wing" configuration. The presentation material shows how to combine the results from different experimental and numerical techniques to support understanding a specific interference phenomenon. At the same time, focus is shed on the configurations with arrays of adjacent propellers since they can be subjected to aerodynamic interactions, which affect the far-field noise. Since the experimental results of the adjacent propellers and the analytical model of the configuration over-the-wing are under revision, not all presented material is included in the lecture notes, but only that open to the public.

I. Installation effects on canonical test-cases

A. Array of adjacent propellers

New aircraft propulsion configurations are being explored to meet the objectives for low noise and pollutant emissions [1]. For several applications, which range from mid-range aircraft to the recently emerging urban-air mobility, the Distributed Electric Propulsion (DEP) concept offers several benefits, including the potential to increase aircraft propulsive efficiency and reduce the community perceived noise [2]. Allowing the thrust to be generated through an array of propellers distributed along the wingspan [3–5], the most relevant benefits are the spanwise lift augmentation [6], and the increase of low-speed performance [7]. Dissecting the total thrust in multiple components makes the system compatible with electric motors, paving the way for more flexible and futuristic designs such as the Helios Prototype Flying Wing by NASA. Previous studies have focused on multiple propellers under hovering conditions due to the detrimental effect on thrust generation of their proximity, which causes a loss of up to 8% [8, 9].

A recent study by de Vries *et al.* [10] showed that adjacent propellers in cruise conditions determine an efficiency loss with respect to the isolated-propeller case of 1.5% for a tip clearance equal to 4% of the propeller radius. Furthermore, it was shown that the time-averaged evolution of the slipstreams was not drastically affected when propellers were located close to each other. One of the exciting research questions on this topic concerns determining the link between the slipstream's deformation, blade unsteady load generation, and far-field noise. The existence of this link can simplify the analysis of either experimental or numerical data without having to enormously increase the computational or experimental costs to obtain the most realistic setup. For example, it has been shown that by decreasing the separation distance among propellers, an emitted sound increase is measured for both tonal and broadband components [11]. Tip-on-tip interaction would induce non-uniform inflow conditions leading to periodic loads that radiate tonal noise [12] in all directions. Broadband noise related to turbulence interactions is instead due to the trailing-edge scattering of the turbulent boundary layer. The second question is whether the interaction between different rotors can be leveraged to reduce the overall noise of the system. This requires understanding the effect of the relative phase angle between the three propellers. It has been suggested that, by synchronizing the azimuthal position of two or more rotors, it is possible to partially cancel the sound emissions in specific directions due to destructive interference [13, 14]. Pascioni *et al.* [15] experimentally obtained a decrease of 6 dB at the rotor's Blade Passing Frequency (BPF), by accurately selecting the phase angle and with a maximum nominal rotational speed deviation of less than 0.5%. Zhou and Fattah [16] also observed that the phase angle between two propellers can affect their sound emissions up to 10 dB. While the relation between the noise reduction and the phase angle is known, the effect of unsteady aerodynamic interactions remains unexplored in the literature, especially in forward-flight conditions. In fact, the relative positioning of the

blades affects their loading and thus the acoustic emissions. Finding the link between the aerodynamic interference effects and additionally providing a physical understanding of why the sound radiation is being modified helps evaluate different configurations, avoiding carrying out additional experimental and numerical activities. In the following, simulations based on a Lattice-Boltzmann Method hybridized with a Very Large Eddy Simulation (LBM/VLES) model for turbulence are carried out to explain the experimental results obtained from a similar setup in the Low-Speed Low-Turbulence Facility of TU Delft.

B. Over-the-wing propeller

Tiltable wings and fixed-pitch (ducted or open) rotors are commonly used in vertical take-off aircraft configurations to provide flexibility for take-off and landing. This results in a complex flight envelope, including vertical take-off, hover, transition, climb, and cruise phases [17]. During the transition phase, the lift force gradually shifts from the propulsive thrust to the wing's circulation. Tilt-wing vehicles generally feature an array of propulsors arranged along the wing. A widely-used configuration is the Leading-Edge Distributed Electric Propulsion (LE-DEP) layout, where rotors are mounted on pylons along the wing's leading edge, aligned with the chord. The induced flow from the rotors increases the wing's lift curve slope, maximum lift coefficient, and stall angle [18, 19]. An alternative to LE-DEP is the Over-The-Wing Distributed Electric Propulsion (OTW-DEP) configuration, where propulsors are mounted above the suction side of the wing. This setup has both beneficial and adverse aerodynamic effects, but overall, it has shown promise in improving aero-propulsive efficiency at the aircraft level. According to the study by de Vries *et al.* [20], OTW-DEP achieved an efficiency increase of up to 9%, with an uncertainty of ± 5%, when compared to isolated propulsion-wing systems. In terms of aeroacoustics, OTW-DEP configurations are considered superior to LE-DEP because the wing can potentially shield rotor noise, thus reducing flyover noise [21]. Focusing on the aerodynamics of an OTW-DEP system, the flow is accelerated over the suction side of the wing by both the upstream and downstream sections of the rotor stream tubes, which lowers the static pressure. This has a positive effect on the system's aerodynamic efficiency. Müller *et al.* [22] reported an 8% increase in the lift-to-drag ratio for an OTW propeller, resulting from a lift increase and a reduction in (pressure) drag. Perry *et al.* [23] investigated the effect of propeller tip speed on aero-propulsive forces, noting increases in lift force, lift-slope, yawing moment, rolling moment, and nose-down pitching moment with rising propeller tip speed. Additionally, Marcus *et al.* [24] found that the lift increase is sensitive to the chordwise position of the propeller. When the propeller is positioned closer to the trailing edge, it maximizes the lift by creating a larger area of reduced surface pressure (increased suction) upstream of the propeller. However, others have reported drag increases due to the presence of the propeller [25], while some have shown that drag is minimized when the propeller is positioned near the airfoil's maximum thickness [26, 27]. Propeller placement is critical, as the resulting static pressure distribution on the wing can lead to flow separation, especially when the propeller is placed upstream of a region with a strong adverse pressure gradient, such as one induced by a deflected flap. In the lecture the experimental setup is discussed of a campaign with over-the-wing propellers that was performed at the Netherlands Aerospace Centre (NLR) in Marknesse, together with a analytical model. The analytical model presented in the lecture is not yet published, and therefore not included in the lecture notes. The experimental results were previously published in [28, 29].

II. Experimental setup discussed in the lecture and data availability

A. Adjacent propellers setup challenging questions

The experiments were carried out at the Low-Speed, Low-Turbulence Tunnel (LTT) located at Delft University of Technology [30]. This wind tunnel is a closed-circuit type with a maximum freestream velocity of 120m s^{-1} and turbulence levels below 0.04% for the freestream velocity used in these experiments. The LTT aeroacoustic test section (Fig. 1) was used for the experiments. It is a special section with lined side panels and a microphone array recessed from a Kevlar panel. The test section has an octagonal cross-section with dimensions of 1.25m in height, 1.8m in width, and 2.6m in length. Its floor and ceiling were covered with 3cm Basotect melamine foam during acoustic measurements. The setup consisted of an array of three six-bladed steel propellers, named XPROP-S, with a radius of R = 101.6mm. In addition, a fourth propeller, with a mirrored version of the original propeller, was used to invert the rotation direction of the middle propeller and mimic a counter-rotating configuration. These propellers were installed on the leading edge of an unswept, untapered wing model featuring an NLF-Mod22(B) airfoil. The wing has a chord of 0.3m and a span of 1.248m. The propellers were powered by brushless DC electric motors (Lehner LMT 2260/40). Each motor was controlled by a dedicated PWM-controlled trapezoidal electronic speed controller (ESC) and an externally

programmable 5 kW DC power supply. The motors were enclosed in an aluminium nacelle, angled downwards at a 5° angle relative to the wing's chord.

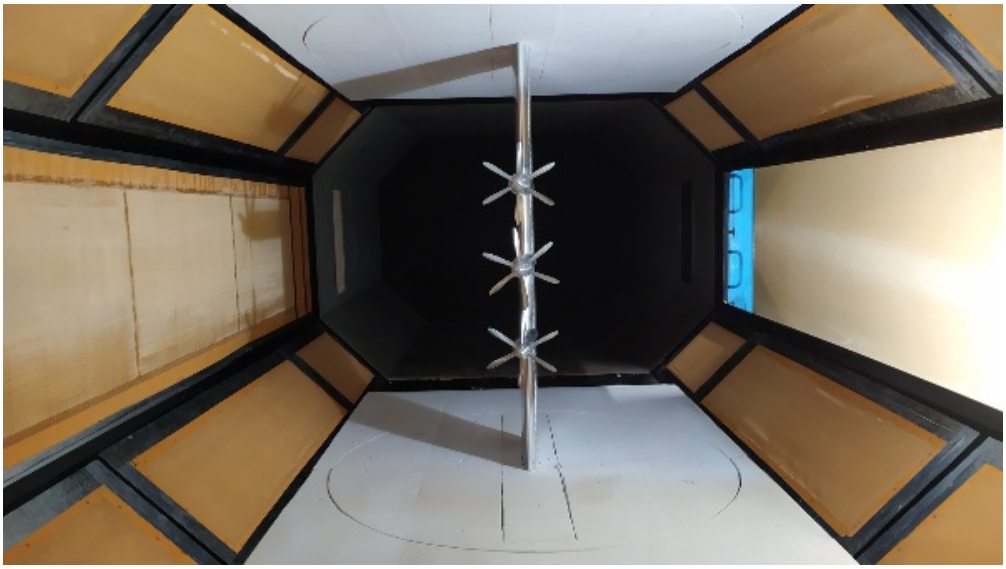


Fig. 1 LTT aeroacoustic test section.

Fig. 1 displays a Kevlar window on the right-side panel of the aeroacoustic test section, behind which a microphone array is installed. The right and left side panels can be switched, allowing acoustic measurements to be taken on both sides. The measurements were conducted at a nominal freestream velocity of 30 m/s. The blade pitch at 70% of its radius was kept at 30°. This pitch angle was preferred over larger angles as it allowed for higher thrust coefficients and blade tip Mach numbers, making it easier to identify both aerodynamic and acoustic interaction effects in the experiment. The propellers were tested at an advance ratio of $J = 0.8$ (184.5Hz), but measurements were also performed at $J = 1.0$ (147.6Hz). The rotational speed and the relative blade phase angle between propellers were controlled with in-house custom-made software. The relative blade angles ranged from 0° to 50° in 10-degree intervals. Random-phase measurements were also performed by increasing the rotational speed of the side propellers by 0.03Hz relative to the middle propeller. This offset corresponds to a change of less than 0.03% in the advance ratio, which has a negligible effect on the propeller's performance. The tip clearance between propellers was 5mm, approximately 5% of the propeller radius. In order to simulate a counter-rotating configuration, the middle propeller was substituted with a mirrored version of the original propeller, as previously mentioned. The wing's angle of attack ranged from 0° to 10°. Lastly, measurements were also obtained using a single propeller mounted on one of the three nacelles to distinguish between interactions with adjacent propellers and interactions with adjacent nacelles. However, due to time constraints, isolated configurations (which involved only one propeller and no adjacent nacelles) were not tested. An overview of test conditions is presented in Table 1. Various measurement techniques were used, though the lecture focused solely on the acoustic data. Acoustic measurements were taken using a phased microphone array composed of 64 GRAS 46BE microphones. The array has an elliptical shape, measuring 1.6m in the streamwise direction and 0.4m vertically. The microphones were set back 15cm from the Kevlar side wall and mounted on a solid plate that was lined with 5cm of melamine foam. Each measurement lasted 30s, with a sampling rate of 51.2kHz. To gather data on slipstream deformation downstream of the setup, a wake rake equipped with both total and static pressure probes was utilized. This rake was positioned one chord-length behind the wing's trailing edge, aligned with the middle propeller. It was traversed vertically in the spanwise direction at 10mm intervals. In the normal direction, the wake rake was centered on the wing wake, and measurements were taken at three specific points: −99mm, 0mm, and 99mm from the wake center. This setup provided a resolution of 3mm within 40mm of the test section centerline. The pressure ports were linked to the same electronic pressure scanner used for the pressure taps, with an identical measurement time. The wake rake and its support structure were only present during slipstream measurements and removed at all other times.

From the results of the experiments, it was observed that changes in the phase angle impact the noise in a distributed-propeller system. The measured noise changes are attributed to an aerodynamic interference between adjacent propellers, given that the result of the interference pattern seems minimal on the microphone wall. Even at

higher angles of attack, adjusting the phase angle effectively reduced the overall noise footprint. This could not be easily explained without an numerical analysis of the flow and acoustic footprint.

Table 1 Test conditions and configurations.

Parameter	Evaluated values
Freestream velocity [m/s]	30
Blade pitch at 70% of the blade radius [deg]	30
Advance ratio [-]	0.80, 1.0
Relative blade-phase angle [deg]	random, 0, 10, 20, 30, 40, 50
Rotation direction	co-rotating
Tip clearance [mm]	5
Angle of attack [deg]	0, 2, 5, 8, 10
(P)propeller/(N)acelle configuration	3P + 3N, 1P + 3N

Despite the detailed analysis of the results cannot be disclosed yet, the full dataset is publicly available on the Zenodo repository through the following link: `https://doi.org/10.5281/zenodo.8307371`. It consists of three folders: Acoustics, Aerodynamics, and Geometry, each containing relevant data in acoustic, aerodynamic, and CAD file formats, respectively. The corresponding README and .txt files are also included within each folder.

B. Over-the-wing propeller, the setup and interactions

For this configuration the experimental setup focuses on the trade-off between acoustic and aeropropulsive performance that can be achieved by varying the propeller positions on top of a wing, and on the aerodynamic and propulsive loading related to the transition from vertical to forward flight conditions. The experiments were performed in the Aeroacoustic Wind Tunnel (AWT) facility at the Netherlands Aerospace Centre (NLR) in Marknesse, see Figure 2. The facility consists of an anechoic chamber (9 x 8 x 6 m), yielding an acoustic absorption rate of 99% above 200Hz. To increase the quality of the aerodynamic measurements, a closed test section was used, limiting the turbulence intensity to a maximum of 0.01% at a free-stream velocity of 20 m/s.

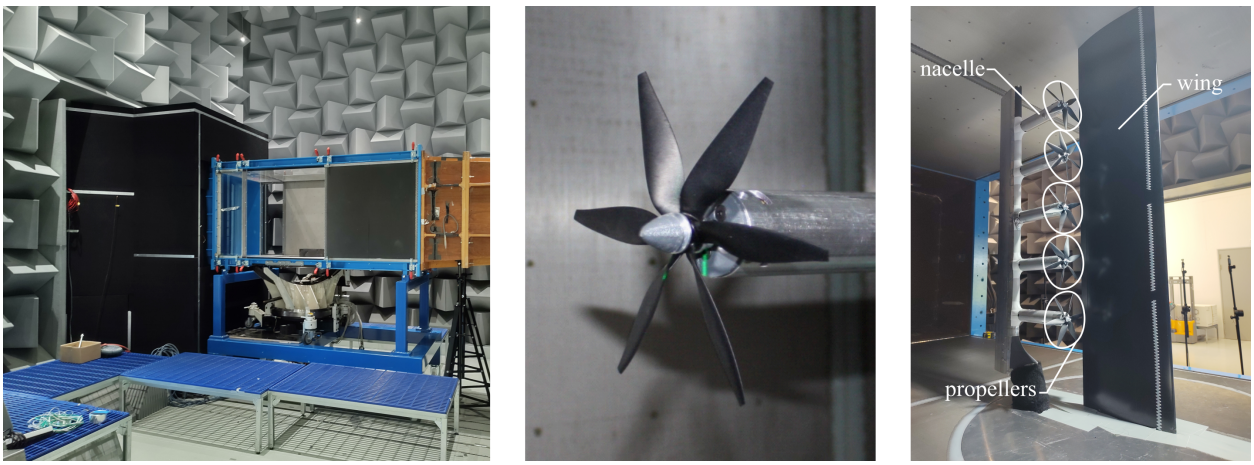


Fig. 2 Side-by-side rotor setup of configuration B3-VTOL.

A F15 wing model was mounted vertically on a turntable in the floor of the closed test section, as shown in the right image of Figure 2. The wing's chord comprises 240mm and the boundary layer was tripped at 10% chord on both the suction and pressure side. Over the suction side of the wing, a sting was connected to the same turntable as the wing. The sting serves as a support structure for five, span-wise distributed nacelles and aligns each nacelle's axis to the wing's chord direction. Inside each nacelle, a brushless in-runner motor drives a custom design six-bladed propeller (radius of

63.5 mm) at a shaft frequency of 383 Hz. The blade design of this propeller is based on a benchmarked version for low-Reynolds application derived from a NACA4412 airfoil [31]. The propeller has been manufactured with CNC out of aluminum with 0.02 mm precision, and cured to avoid material relaxation and oxidation. The experiments have been split into three separate test campaigns, with an increasing degree of complexity of the model. First of all, the single isolated propeller is tested, then a single over-the-wing propeller. The isolated propeller tests concern a fixed rotational speed and angle of attack. The free-stream velocity is varied to measure multiple advance ratios ranging from hover (J = 0) to cruise conditions (J = 0.6). The experimental conditions for the isolated propeller are summarized in Table 2.

Table 2 Operating conditions isolated propeller

rotational speed Ω (Hz)	383
free-stream velocity V_∞	[0, 7.3, 14.6, 21.9, 29.2, 36.5]
advance ratio J	[0, 0.15, 0.3, 0.45, 0.6, 0.75]
angle of attack α (°)	0
(3/4)R rotor blade chord Reynolds number Re_b	60,000
tip Mach number M_t	0.42

A wide range propeller advance ratios J and inflow angles α are investigated for the installed configuration. Furthermore, three different propeller positions along the wing's chord line are considered. The experimental conditions for the single over-the-wing propeller are summarized in Table 3.

Table 3 Operating conditions single OTW propeller

rotational speed Ω (Hz)	383
free-stream velocity V_∞	[0, 7.3, 14.6, 21.9, 29.2]
advance ratio J	[0, 0.15, 0.3, 0.45, 0.6]
angle of attack α (°)	[0, 2, 4, 6, 8, 10, 12, 14, 16]
rotor tip gap y/R	[0.17, 0.27]
rotor chordwise position x/c	[0.3, 0.6, 0.9]
rotor spanwise position z/R	±[0, 0.08, 0.16, 0.32, 0.48, 0.64, 0.8]
(3/4)R rotor blade chord Reynolds number Re_b	60,000
wing chord Reynolds number Re_c	120,000 - 480,000
tip Mach number M_t	0.42

A wide range of measurement techniques are conducted. For the center nacelle (i.e. the mounting of the center propeller), the brushless motor is connected to the nacelle using two parallel-mounted uni-axial FUTEK LSB205 load cells and a FUTEK QTA141, which allows for thrust and torque measurements on the propeller. The load cells are excited with 7 volts of direct current (VDC) by a single power supply. Repeated measurements showed a maximum deviation of 2% for thrust and 5% for torque. The integral loading of the wing is measured by a custom-made six-component force balance. In the lift and drag direction, the balance has a capacity of 1800 N and 325 N, respectively. The uncertainty as a percentage of the full load range is 0.13 % for the lift direction and 0.8 % for the drag direction. Acoustic measurements were performed to both measure the increase in noise of the propeller and to quantify the effect of noise shielding. The noise of the propeller is measured using a microphone array consisting of 64 microphones. The array is positioned outside the test section at a distance of 0.70 m and angled towards the suction side of the wing. Additionally, three free-field microphones are positioned outside the test section on the pressure side of the wing to investigate the potential of noise shielding by the wing. The free-field microphones are positioned at a distance of 2 m from the center of the test section. All microphones are sampled at a frequency of 41 kHz for a time duration of 20 s for each data point. In the center span position of the wing, 59 static pressure taps are fitted. Two additional, coarser spaced, pressure tap rows are positioned at 25%- and 75%-span to evaluate the two-dimensionality of the flow. All pressure measurements are averaged over 20 s. For a number of data points, the propeller is traversed along z-direction (i.e., spanwise), in steps of 10 mm to a maximum displacement of 50 mm (0.8 R) in both positive and negative z-direction. This allows for a surface

pressure reconstruction to investigate spanwise variations. The flow at the inflow of the single over-the-wing propeller is characterized using stereoscopic particle image velocimetry (sPIV). The flow is seeded with DEHS tracer particles (τ = 2 μs) which are illuminated by an evergreen laser (200 mJ/pulse) in a sheet of 3mm thickness. Illumination is performed at a rate of 15 Hz and the duration for each pulse (pulse width) is δt = 25 ns. Recording is performed by two sCMOS cameras (Imager sCMOS CLHS) placed outside the section at a distance of 0.6 m from the center of the measurement region. The camera is equipped with an objective of focal length f = 50 mm, set at numerical aperture f# = 8. The resulting field of view spans 19 x 25 cm^2 (3 R x 4 R). System synchronization is obtained with a LaVision Programmable timing unit (PTU X) and each measurement comprises at least 300 recordings for a time duration of 20 s. An overview of the illumination and imaging conditions is presented in Table 3.

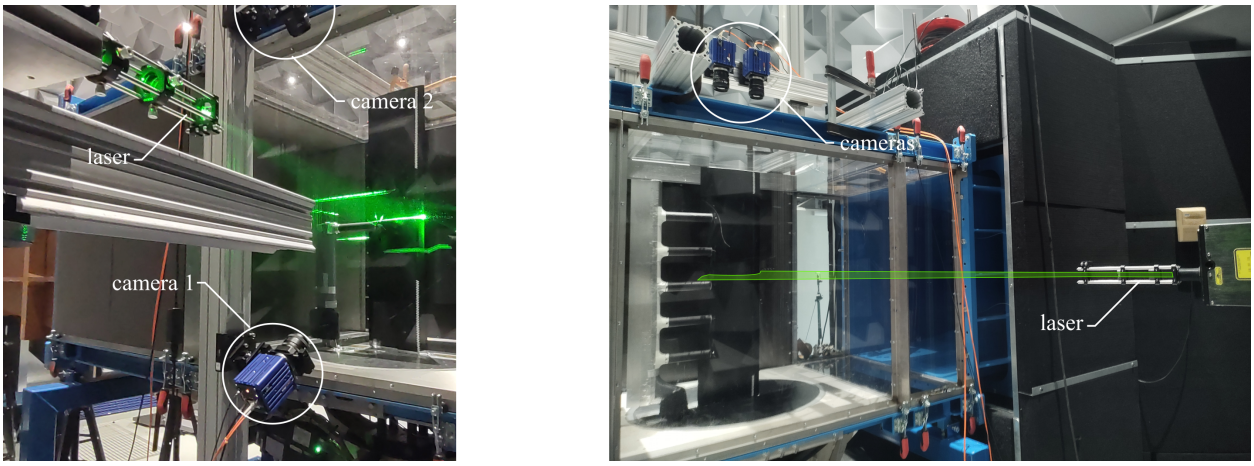


Fig. 3 Stereoscopic PIV setup (left) and 2D2C PIV setup (right) used for the aerodynamic investigation of B3-FLap.

For this specific setup an analytical model is built which separates the effect of the wing on the propeller as slipstream tube deformation from the impact of the propeller on the wing, developing a boundary layer with an unsteady inflow change. Although the comparison and the analysis are under revision and cannot be presented here, the datasets the analysis is based upon are publicly accessible on the Zenodo repository by using the following link: `https://doi.org/10.5281/zenodo.8283630`. The B3-FLAP contains four folders: "CAD", "IsoPropeller", "SinglePropeller" and "Distributed propeller". The "CAD" folder contains the propeller airfoil sections and CAD files while the other three folders contain measurements of the three test campaigns for B3-FLAP. Each measurement folder has a sub-folder containing either the acoustic, pressure, loading or velocimetry data. The corresponding metadata and README files are included within each of these sub-folders.

III. Numerical study of the aerodynamic installations effects

A. Array of adjacent propellers

The numerical results follow from the setup presented in [32]. The commercial CFD/CAA software SIMULIA PowerFLOW®, version 6-2021-R2, solves the flow and clarifies the research questions associated with the array of adjacent propellers. It solves the discrete LB equation for the distribution function $f(\boldsymbol{x}, \boldsymbol{v}, t)$, which represents the probability density of particles with velocity $\boldsymbol{v}$ at location $\boldsymbol{x}$ and time t. A D3Q19 stencil, which utilizes 19 discrete velocities in the 3 spatial dimensions, is considered, together with a regularized collision operator based on the Bhatnagar-Gross-Krook (BGK) collision model [33]. A Cartesian grid with cubic volumetric elements (voxels) is used to solve the LB equations, while planar surface elements (surfels) are used to discretize the surfaces of solid bodies within each voxel that intersects the wall geometry. The solver employs a VLES approach to model the effects of the unresolved scales of turbulence. A two-equation transport model based on the k-ϵ renormalization group theory [34] is used to compute the turbulent relaxation time associated with time scales of the resolved sheared flow field [35]. To reduce the computational cost, a pressure-gradient extended wall model is used to approximate the no-slip boundary

condition on solid walls. This model is based on the extension of the generalized law-of-the-wall model to take into account the effect of the pressure gradient. The far-field noise is computed *via* an impermeable FW-H formulation, known as Farassat's Formulation 1A [36], solved in forward time [37]. The computational test case is three adjacent propellers, as shown in Figure 4(a)).

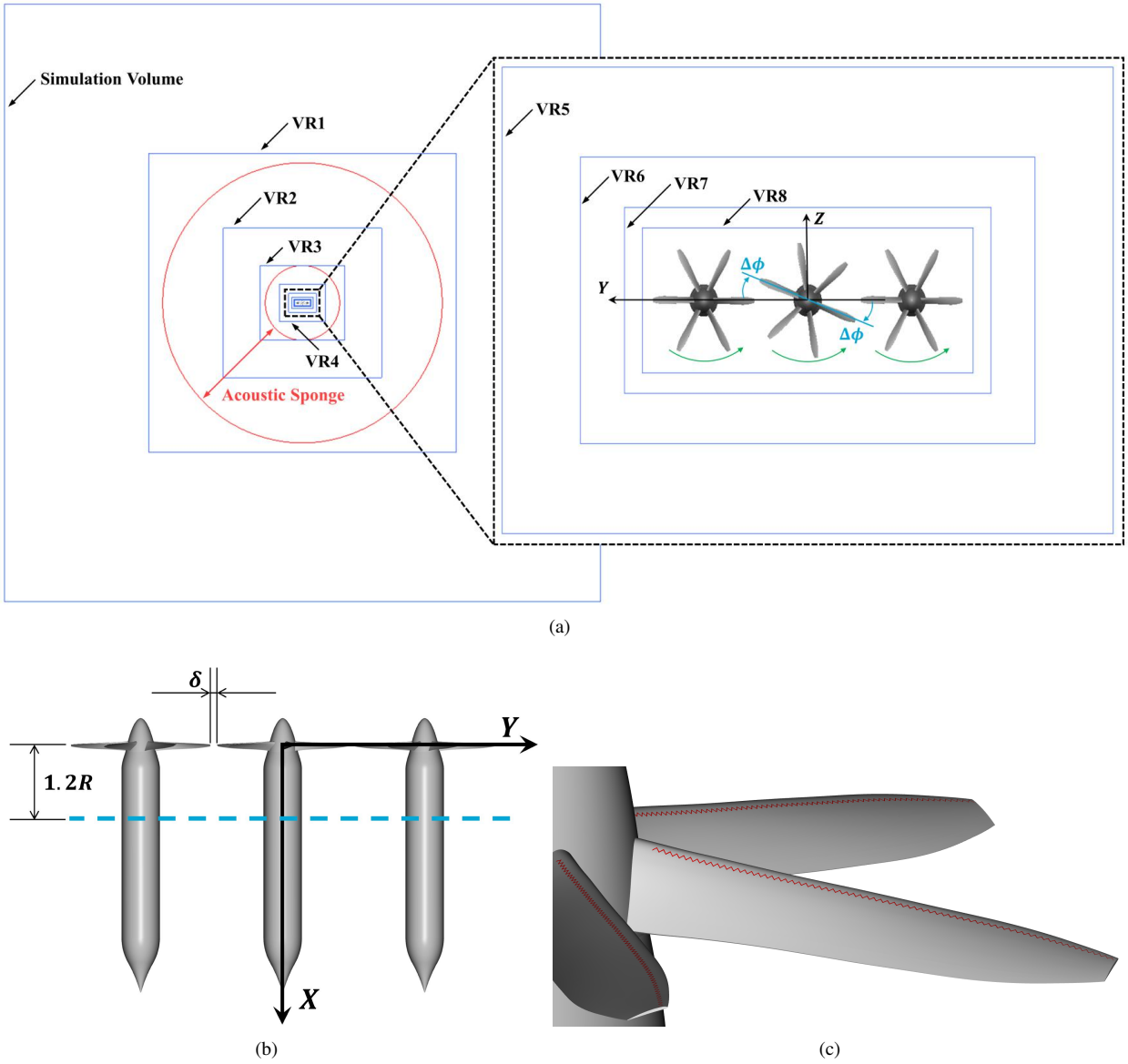
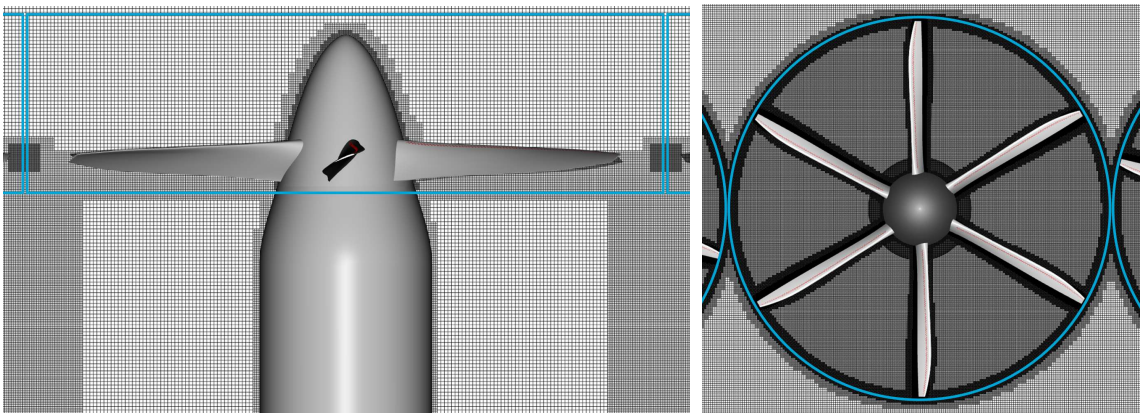


Fig. 4 (a) Front view of the computational domain with the Variable Resolution (VR) mesh regions and the global reference frame. (b) Top view of the three adjacent propellers with wake survey plane location in a dashed line. (c) Close-up on the zig-zag trip applied on the blades.

The TUD-XPROP-S propellers feature six blades and a diameter $D = 0.2032$ m [10]. The pitch angle is equal to 30° at 70% of the radius ($r/R = 0.7$, where r is the local radial location and R is the propeller radius), whereas the root chord length of the blades is $c_r = 16.287$ mm. More details concerning the geometry of the propeller, such as the pitch angle and chord distributions along the blade span are given in Ref. [10]. The nacelles are designed with a length corresponding to $3.7R$ and with a tapered termination to minimize any possible disturbance to the flow field around the rotors. Three identical propellers are distributed along the Y-axis, with tip clearance of $\delta = 0.02D = 4.064$ mm, as shown in Figure 4(b). In the same figure the Global Reference System (GRS) (X, Y, Z) is also introduced. Figure 4(a) shows a

configuration with a co-rotating direction of the propellers (anticlockwise) and a relative phase angle of $\Delta\phi = 15°$. In order to investigate the influence of the relative phase angle on the aerodynamic and acoustic performance, an additional configuration with $\Delta\phi = 0°$ is investigated. The propellers are operated at free-stream velocity $V_\infty = 30\ \mathrm{m\,s^{-1}}$, directed along the X-axis, and at an advance ratio $J = V_\infty/(nD) = 0.8$, where n is the number of rotations per second. The Mach number at the tip is equal to 0.357 and the Reynolds number at the tip is 5.66×10^4, given that the chord at the tip is equal to 6.8 mm. The free-stream static pressure and temperature are $p_\infty = 101330$ Pa and $T_\infty = 288.15$ K. The inlet turbulence intensity is set to a value of 0.04%, similar to the experiments. The rotation time is equal to $T_{rot} = 5.41867 \times 10^{-3}$ s. The simulation volume, depicted in Figure 4(a), is a cubic box whose side faces are placed $64D$ away from the GRS origin. To prevent acoustic reflections at the outer boundary, an acoustic sponge, i.e. an anechoic outer layer, is defined by two concentric spheres of radius $8D$ and $30D$, respectively, centred at the GRS origin [38, 39]. In this region, the viscosity increases up to a constant value at radial locations larger than $30D$. A total of 15 Variable Resolution (VR) regions are employed; the change in resolution between adjacent VR regions is equal to 2. The first 8 VRs are defined as the boxes shown in Figure 4(a) (the simulation volume being set at VR0), where the correct scaled dimensions are reported and where the refinement level is increased moving toward the GRS origin. In Figure 5(a), three volumes of revolution defining the Local Reference Frame (LRF) of each propeller are indicated with solid lines.



(a) (b)

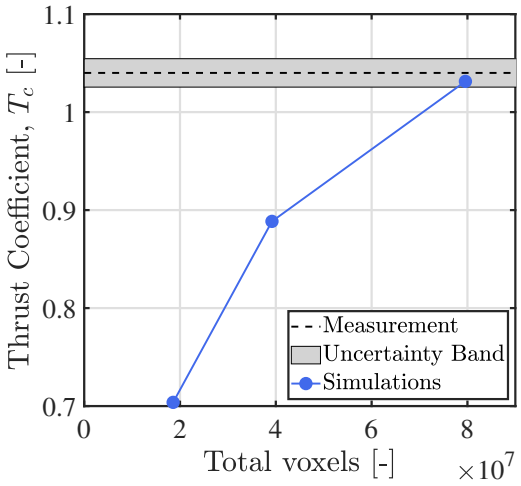
Fig. 5 Near-body grid size with volumes of revolution enclosed by a solid line: top view (a) and front view (b).

Each of the grids contained within these regions slides with respect to the outer stationary grid. Within the revolution volumes, a refinement (VR9) is applied. Cylindrical hollow refinements set to VR9 can also be observed: these are used to better discretize the regions enveloping the slipstream helical paths. VR10 is applied around the blade and spinner surfaces and to ring refinement regions following the blade tip motion, as illustrated in Figure 5(b). The latter approach is needed to allow a minimum of 4 voxels to discretize the non-rotating gaps between the tips of the blades. VR10, VR11, and VR12 are applied on the blade surfaces, where a fine discretization is needed to capture the surface pressure fluctuations. The nacelles are enveloped by VR9. The finest VR13 and VR14 envelope the zig-zag trip device that is located at 10% from the blade leading edge (see it in Figure 4(c)). This is done to discretize the trip thickness with about three voxels, as suggested in Ref. [40]. A physical zig-zag trip is applied on the blade suction side to force turbulent boundary-layer transition and cause the VLES to switch from a modeled- to a resolved-scale modality. For the finest grid case, a total of about 225.5 million voxels are used to discretize the case, with a resolution at VR14 of 900 voxels per characteristic length (c_r). This leads to the smallest voxel size of 1.79445×10^{-5} m. The isolated-propeller case involves the same setup and characteristics as the distributed one described above, with about one-third of the total voxel count. The acoustic data is sampled at 33.218 kHz on the solid FW-H integration surfaces, corresponding to the propeller blades.

IV. Results from the numerical model

Figure 6(a) shows the grid convergence study for the isolated-propeller case. The value of the thrust coefficient is defined as $T_c = T/(q_\infty \pi R^2)$, where T is the thrust and q_∞ is the upstream undisturbed dynamic pressure. As can be

seen, the trend gets closer to the measurements [10], until a difference of 0.9% is achieved with the finest mesh. The latter is then used to conduct the following analyses. In order to reliably compare the simulated SPL, the low-fidelity methodology present within the Opty∂B toolkit is employed, based on a Blade Element Momentum Theory (BEMT) model to compute the radial distribution of forces [40], and a time-domain FW-H formulation based on a compact dipole and compact monopole formulation [41]. Figure 7(a) shows the directivity of tonal sound at the first BPF calculated, by means of the BEMT/FW-H approach, in the XY plane, namely the one containing the axis of rotation and perpendicular to the plane of the rotor. In this work, L_p is always calculated on this plane and at $10D$ from the GRS origin on this plane, unless differently specified. According to propeller noise theory [42], steady-loading noise and thickness noise dominate the sound emissions generated by an isolated rotor for observers located in the plane of the rotor. Indeed, one can see the characteristic vertical lobe shape which reaches a maximum for observers placed in this plane. In contrast, the sound directivity reaches a minimum for listeners placed in the direction of the axis of rotation. Notice how the LBM/VLES simulation of the isolated case reports the vertical lobe shape with a deviation of less than 2 dB on the vertical axis. This occurs for both observers placed in the XY plane and those in the XZ plane. This small discrepancy is attributed to unsteady loading effects that are absent in the BEMT + FW-H computation. Since the isolated case is axisymmetric, these two curves should overlap perfectly in both planes. However, on the horizontal axis, in the angular ranges between 330° and 30° and between 150° and 210°, two different trends of L_p directivity are observed. This is because in such directions the contribution of steady loading noise and thickness noise is very low. What remains is due to random acoustic pressure fluctuations of very small magnitude (we are around and below 20 dB). In Figure 7(b), we show the directivity of the calculated SPL for the DP case with $\Delta\phi = 15°$ at the first BPF. This figure depicts the sound emitted by the middle propeller, but it can similarly be shown that even taking into account the contribution of the two adjacent propellers, the loading noise is always far greater than the thickness noise in each direction (minimum difference of 4.4 dB up to 67 dB in the upstream direction).



(a)

Fig. 6 Convergence of the thrust coefficient against the total number of voxels for the isolated propeller.

V. Understanding the aerodynamic interactions

In Figure 8(a), the slipstream development for the isolated-propeller case at a given time instant is reported by means of the λ_2 criterion, computed with a value of $\lambda_2 = -2 \times 10^6\ 1/s^2$. It can be seen that the vortical structures follow a helical path starting from the blade tip and evolving essentially undisturbed downstream of the rotor. Referring to the DP case with $\Delta\phi = 15°$ in Figure 8(b), we do observe that the proximity between the rotors induces a deformation of the vortex structures that become progressively more pronounced moving downstream of the rotor. This interaction is due to the circulations of the vortical structures mutually influencing their trajectories and that of the structures adjacent to them through the generation of an induced-velocity field.

In Figure 9(a), we report the thrust produced by the blades of the simulated propellers as a function of the physical

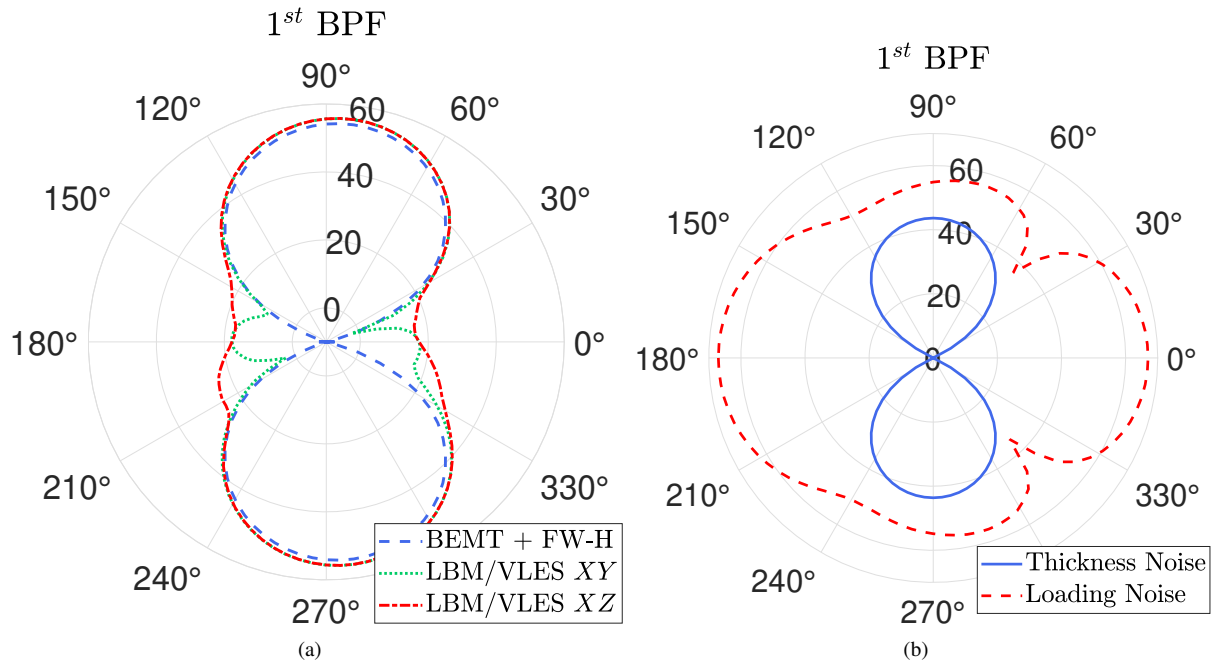


Fig. 7 Far-field sound L_p at the first BPF. In (a), this is computed for the isolated-propeller simulation in XY and XZ planes against the one computed *via* BEMT+FW-H low-fidelity approach. In (b), the contribution of the thickness noise against loading noise is represented for the middle propeller of the $\Delta\phi = 15°$ configuration.

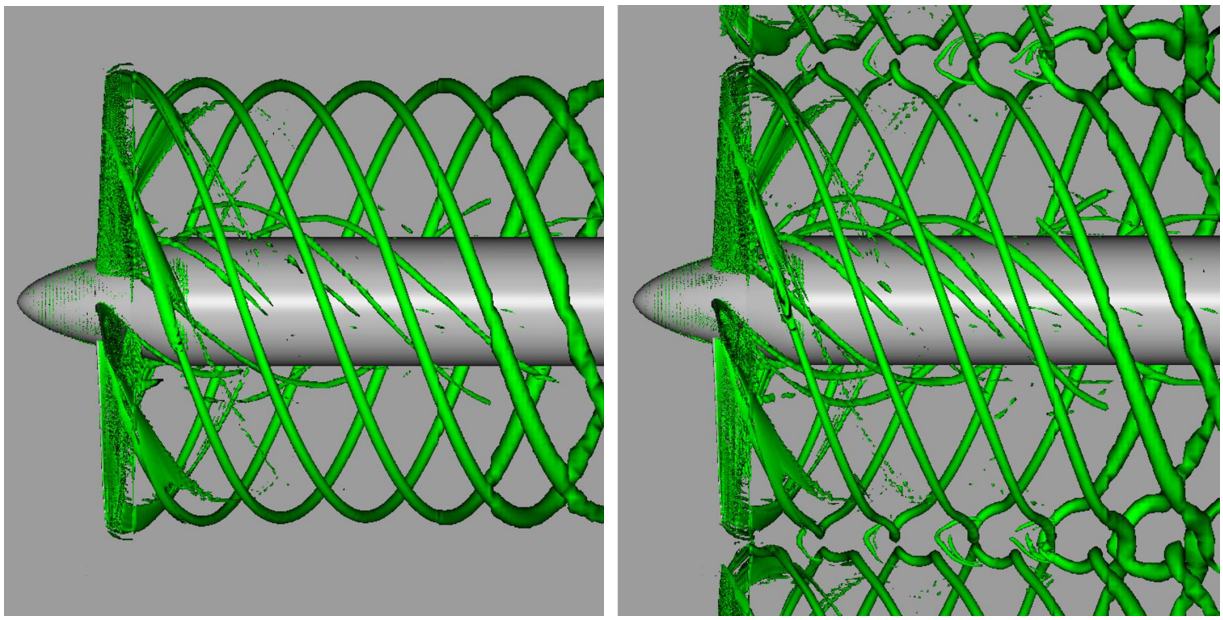
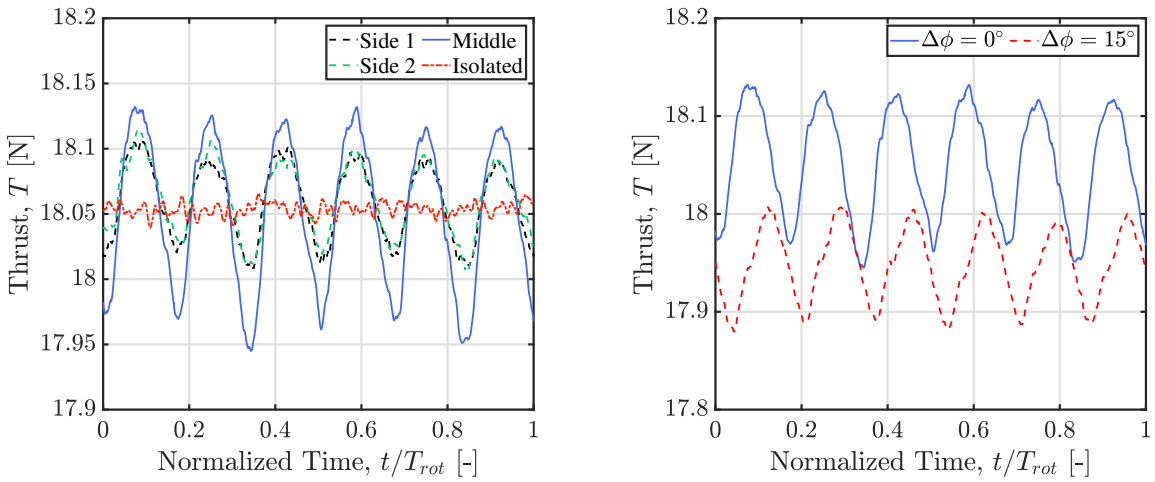


Fig. 8 Isosurface computed through the $\lambda 2$ criterion with a value of $\lambda_2 = -2 \times 10^6$ 1/s^2: isolated-propeller case (a), distributed-propeller case $\Delta\phi = 15°$ (b).

time t normalized by the rotation time T_{rot}. We notice how the isolated propeller generates a relatively constant thrust profile with small fluctuations from the mean value possibly caused by its own wake development. Differently, propellers belonging to the DP case (for instance, the $\Delta\phi = 15°$ case reported in the figure) show greater oscillations



(a) (b)

Fig. 9 (a) Thrust values produced by the blades of the propellers of the distributed configuration (Side 1, Side 2, and Middle) and of the single propeller case (Isolated). (b) Thrust values produced by the blades of the middle propellers for the two analyzed DP cases.

from their mean value. In particular, the side propellers (see Figure 4(b)), present peak-to-peak oscillations of about 0.4% from the mean value, while the middle one exhibits fluctuations of about twice as much. This indicates that the fluctuations are caused by the aerodynamic interactions between the propellers since the middle one interacts on both sides. It is thus shown that the tip-on-tip interaction increases the unsteadiness of the thrust generated by the blades, anticipating an augmentation of noise production, as reported in Section VI. Moreover, consistently with the experimental findings [10], we confirm that the impact of the angle $\Delta\phi$ on time-averaged thrust, and hence on aerodynamic performance, is negligible when compared to the isolated-propeller case, as it was consistently less than 0.75% across all analyzed cases. The propeller's thrust in the middle for the DP configurations is reported in Figure 9(b). The thrust profile is modulated by a sinusoidal pattern that has a periodicity of six times the period of rotation. This is clearly due to the interaction with the blades of adjacent propellers. Furthermore, we may notice the expected temporal phase shift corresponding to 15° compared with the case with $\Delta\phi = 0°$. However, we further remark that the average peak-to-peak ratio for the case with $\Delta\phi = 15°$ is only 0.60%. This means the evolution of the slipstreams affects the magnitude of the tip-on-tip interaction, which becomes a function of the relative phase angle $\Delta\phi$. To investigate how the tip-on-tip interaction impacts the azimuthal and radial distribution of thrust, we calculate the difference between the thrust coefficient of the DP case with $\Delta\phi = 15°$ versus that of the isolated case ($\Delta T_c = T_{c_{\Delta\phi=15°}} - T_{c_{iso}}$) in the rotor plane. The blade is divided into 100 spanwise segments on which ΔT_c is computed.

Figure 10(a) illustrates that for the side propeller (the one located on the positive direction of the Y-axis in Figure 4(b)) the thrust coefficient's azimuthally uniform distribution is disrupted. This happens when the blades come closer to the middle propeller: in the approaching phase, the thrust decreases until it reaches the minimal distance from the middle-propeller blades. After that, the thrust increases again. This process is repeated twice in one revolution for the middle propeller, as shown in Figure 10(b), namely when the blades approach and retreat the side propellers. One notable aspect is that the alterations in thrust occur close to the blade tip, with the highest thrust point located at around 80% of the blade's radius. These adjustments in thrust at the blade tips are distinct from the time-averaged analysis discussed previously, as the decrease and increase in thrust are symmetrical and, therefore, do not influence the propeller's time-averaged performance. However, this pattern is connected to the unsteadiness generated between the propellers, which is crucial for noise generation.

VI. Numerical results, understanding the acoustics

In Figure 11(a), S_{pp} is computed by means of the FW-H impermeable formulation for one microphone located at $X = -10D$ and $Y = Z = 0$, i.e., upstream of the middle propeller. The far-field sound spectrum obtained from the middle propeller of the case with $\Delta\phi = 0°$ is compared with that obtained from the isolated propeller. Three tonal peaks are present in the case with $\Delta\phi = 0°$, at the first BPF and harmonics. These tones are attributed to the unsteadiness

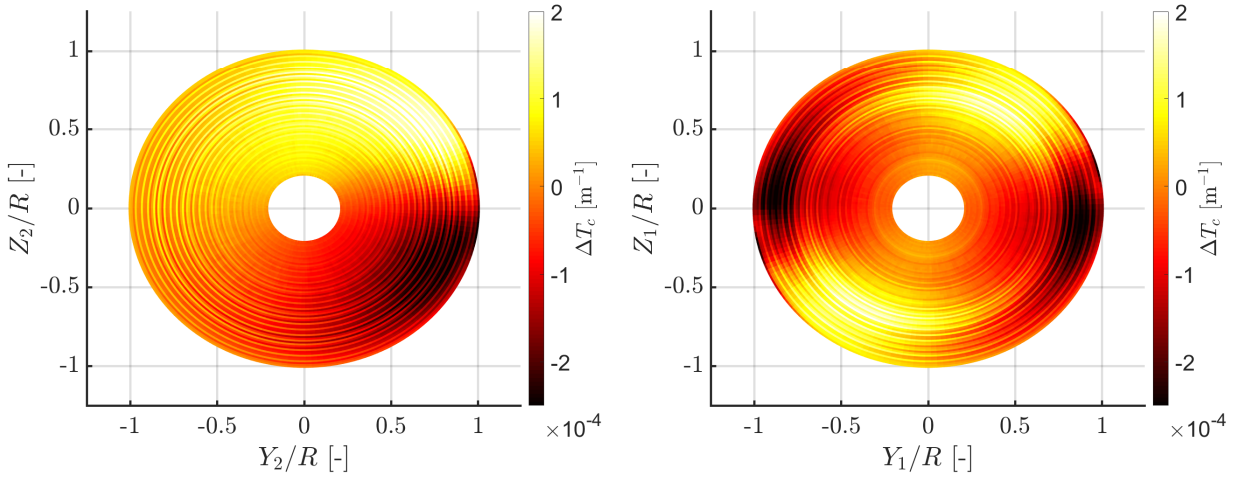


Fig. 10 Thrust coefficient distribution difference (ΔT_c) between the distributed configuration with $\Delta\phi = 15°$ and the isolated propeller. Side1 propeller depicted in (a), Middle propeller depicted in (b).

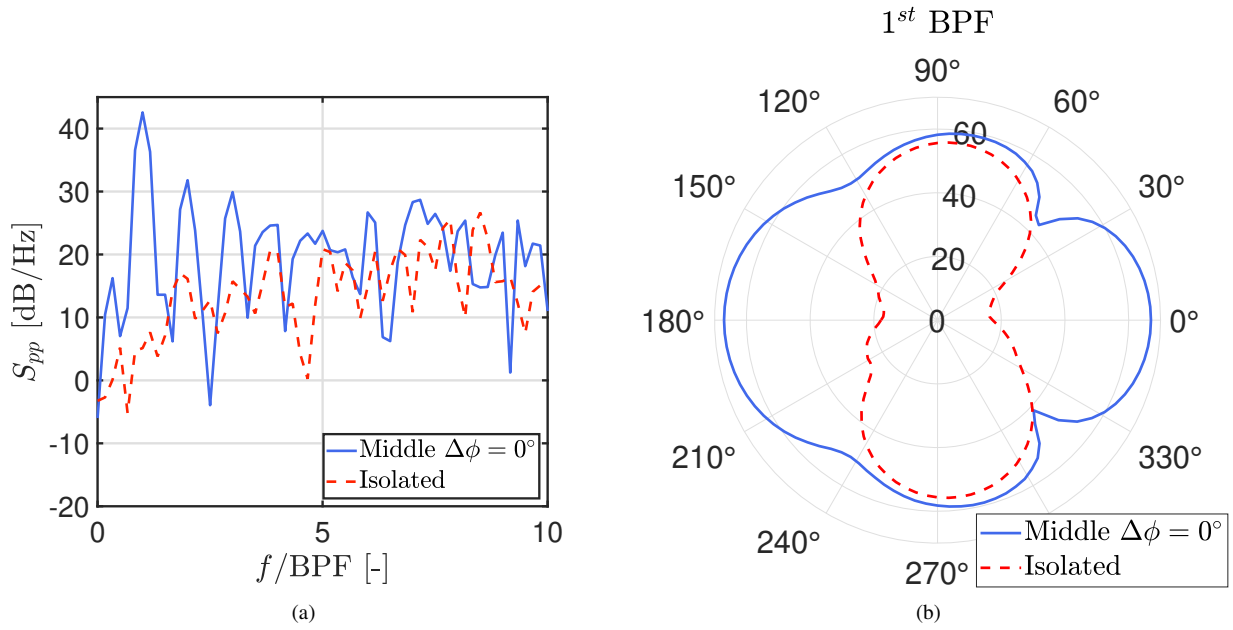


Fig. 11 (a) Far-field noise power spectral density S_{pp} , with microphone position at $X = -10D$ and $Y = Z = 0$; comparison between the distributed middle propeller with $\Delta\phi = 0°$ against the isolated one. (b) Far-field sound L_p directivity plot comparing the distributed middle propeller with $\Delta\phi = 0°$ and the isolated one.

generated by the aerodynamic tip-on-tip interaction discussed in Section V and dominate the acoustic emissions at microphone location. In contrast, the isolated-propeller case presents a sound spectrum without any tonal peaks that stand out visibly from the average broadband level identified by the simulation. This is because the amplitude of steady loading noise and thickness noise is maximum in the plane of the rotor and minimum along the propeller axis, as explained in Section IV. Keeping in mind that the focus of this work is on tonal noise, we ensured that the amplitude of the tonal peaks at the first and second BPFs does not change when the length of the temporal signal, on which the sound

spectrum is calculated, is varied. In Figure 11(b), we compare the isolated-propeller case versus the middle-propeller case when $\Delta\phi = 0°$. We illustrate how the sound pressure level L_p varies in the XY plane with the microphones placed $10D$ from the GRS origin in Figure 4(b). We can see that at 90°, the middle propeller generates sound emissions that exceed the one generated by the isolated propeller by about 2.5 dB. This is attributed to the larger level of flow unsteadiness induced by the proximity of the side propellers. The horizontal directivity lobes that strongly dominate the upstream and downstream directions of the flow are also due to this interaction. As a consequence, we infer that the unsteady loading interaction between adjacent rotors is by far the dominant generating mechanism for this DP configuration, especially upstream and downstream of the propellers.

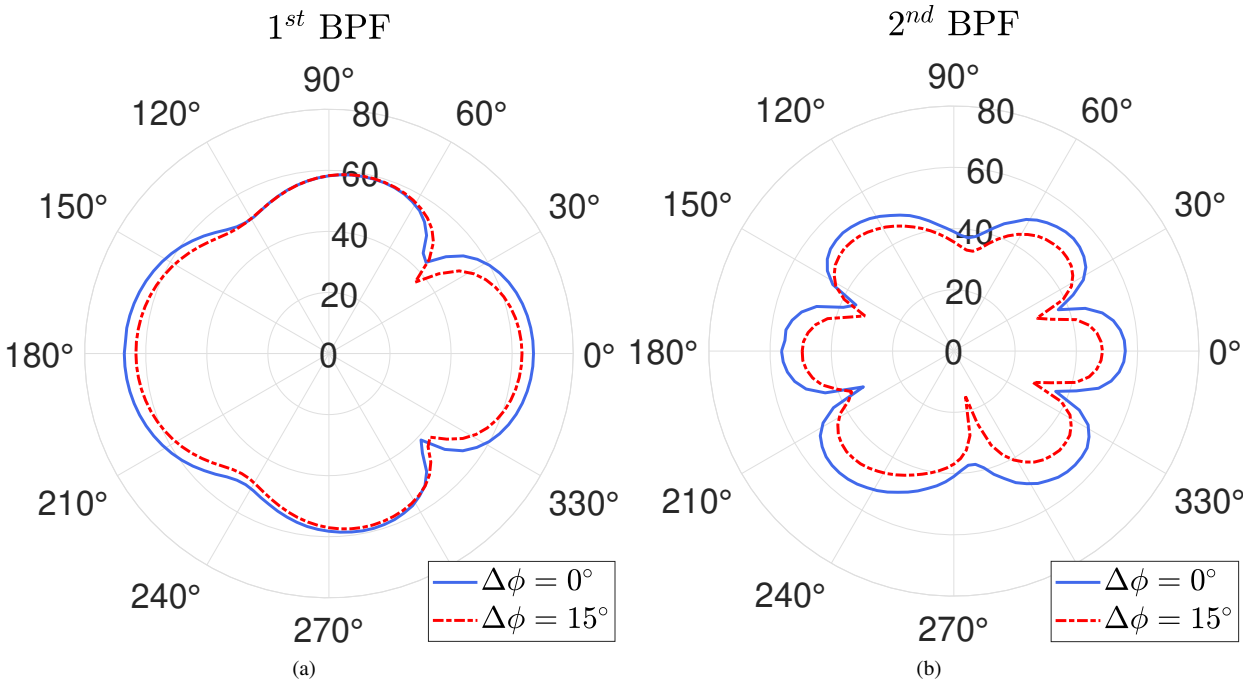


Fig. 12 Far-field sound L_p directivity plot comparing the distributed middle propellers with $\Delta\phi = 0°$ and $\Delta\phi = 15°$. Tones at the first BPF (a), and at the second BPF (b).

In Figure 12(a), we show the effect of employing a different relative phase angle $\Delta\phi$, comparing the tone generated at the first BPF by the middle propeller for the configuration with $\Delta\phi = 0°$ versus the one for the configuration with $\Delta\phi = 15°$. We may observe that generally, the shape of the sound directivity remains very similar between the two cases. However, the case with $\Delta\phi = 15°$ exhibits less noise amplitude in the direction of the axis of rotation by 4.2 dB. This can be explained by the reduced aerodynamic interaction between propellers that occurs in this case, as demonstrated earlier in Figure 9(b). Differently, in the rotor plane, since steady loading noise dominates the sound emission and since the difference in average thrust between the two cases is negligible, we obtain almost the same level of sound emission along this direction. In Figure 12(b), the comparison of the tone at the second BPF for the two DP configurations is depicted. Again, the shape of the directivity lobes is quite similar between the two examined cases. However, the configuration with $\Delta\phi = 0°$ shows higher noise amplitude in all the directions (about 7 dB along the rotation axis direction). This is also caused by the unsteady loading interactions, according to the propeller noise theory [42].

In Figure 13(a), we show the directivity plot obtained by accounting for the three propellers. This is in order to identify whether acoustic interference between the three propellers would significantly change the sound directivity of the tone at the first BPF. However, this does not occur since it retains essentially the same shape of the sound lobes as in the case of Figure 12(a), where only the middle-propeller contribution was included. Similarly, this also occurs in Figure 13(b), where the tonal directivity at the second BPF is depicted. One might expect that there would be other acoustic interaction effects that would change the directivity shape at the first BPF, but this is not the case since the acoustic wavelengths corresponding to the first and second BPFs are large compared to the characteristic distance between the sound sources on the blade or on the blade tips of two adjacent rotors. These frequencies are therefore

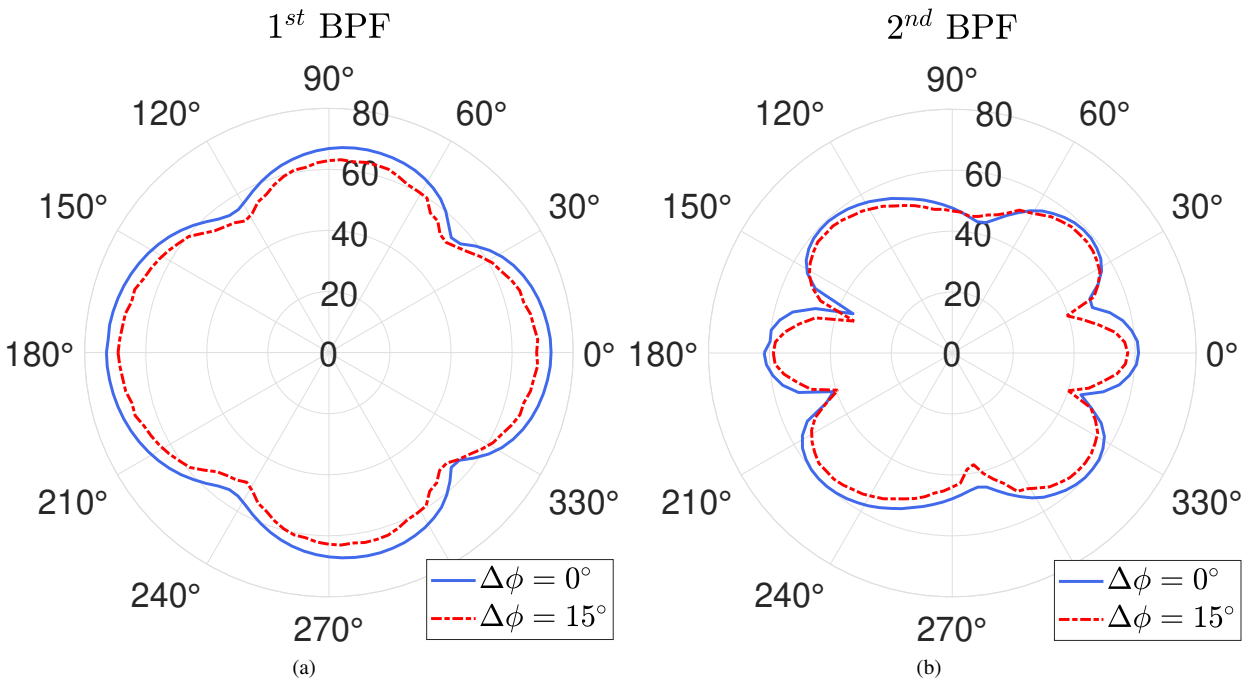


Fig. 13 Far-field sound L_p directivity plot obtained summing the 3 propellers contributions for the 2 analyzed configurations with $\Delta\phi = 0°$ and $\Delta\phi = 15°$. Tones at the first BPF (a), and at the second BPF (b).

acoustically compact and the sound directivity maintains a shape similar to that of the isolated rotor. Hence, it is the unsteady tip-on-tip interaction that determines the sound-emission directivity around the propeller array. However, we remark that along the vertical direction the case with $\Delta\phi = 0°$ radiates about 4 dB more than the one with $\Delta\phi = 15°$. We conjecture that this amplification effect may be due to an acoustic constructive/destructive interference, caused by the relative phase angle $\Delta\phi$. To prove that, we report the acoustic pressure signal as a function of time at the microphone location $Y = -10D$, $X = Z = 0$ for the DP case with $\Delta\phi = 0°$ in Figure 14(a). This is computed removing the mean of the pressure signal $\bar{p}$ as $p' = p - \bar{p}$. We notice that the acoustic pressure signals computed from the three propellers are in phase. Differently, observing the DP case with $\Delta\phi = 15°$, the middle-propeller acoustic pressure signal shows a time shift which leads to a destructive acoustic interference that mitigate the total radiated noise along this direction.

VII. Combining experimental and numerical results

As you might have noticed from the description of the experimental and numerical setups, both are not exactly equivalent. Most prominently, the experiment featured a wing behind the propellers, that was not there in the simulation. Nevertheless, multiple aspects of both experiments are interesting to compare.

The first aspect that can be compared is the noise production in the first BPF in directions from which there are both simulations and measurements. This is the case in the 90° direction, where both experimental and numerical measurements have been carried out. This does require a correction for the different distances of the microphones, which are at 0.9m experimentally and at 2.032m numerically, causing a difference of 7.1 dB. With this correction, the $\Delta\phi = 0°$ case in Fig. 13(a) yields 73.9 dB. The measured result from [30] in Fig. 15 shows a very close match with this.

Besides comparing the magnitude of the noise production, it is even more interesting to investigate whether the experimental and numerical studies capture the same phenomena and trends. Also this can be done using the results in Fig. 15. While the experimental study did not contain a measurement point of $\Delta\phi = 15°$, the difference of 4 dB with the $\Delta\phi = 0°$ case observed in Fig. 13(a) would fit in Fig. 15 very well. The pattern in the results over the different $\Delta\phi$ in Fig. 15 has later been observed in a larger numerical campaign as well, which has been partially published in [14] and will be fully published in a later stadium.

Another important comparison can be done with regard to the directivity. While full directivity plots are not measured experimentally, we can derive from Fig. 13(a) and Fig. 13(b) that the difference in noise between the $\Delta\phi = 0°$

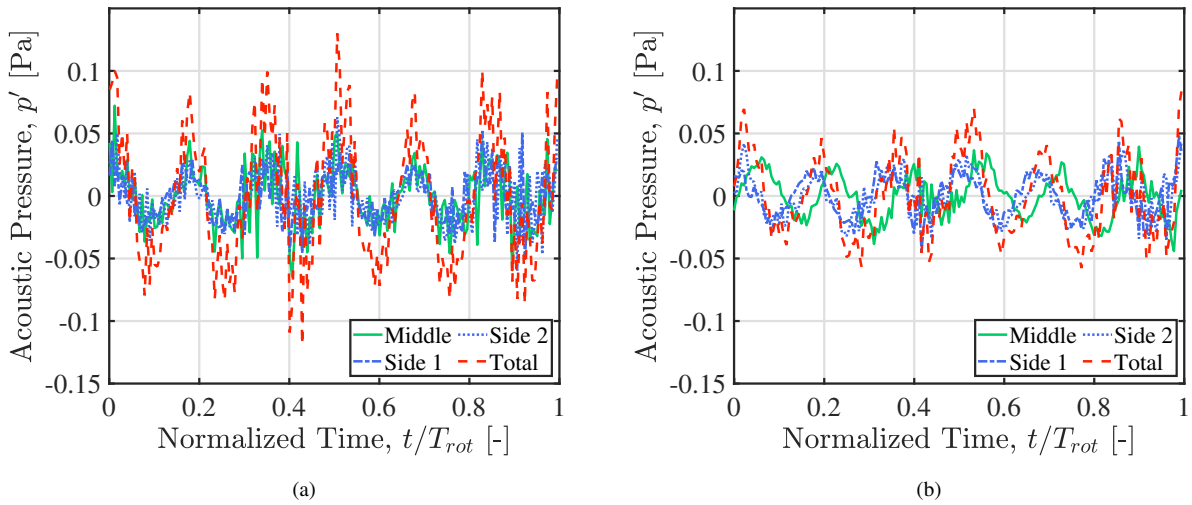


Fig. 14 Acoustic pressure signal as a function of time at microphone location $Y = -10D$, $X = Z = 0$; in (a) the DP case with $\Delta\phi = 0°$ is depicted, in (b) the DP case with $\Delta\phi = 15°$.

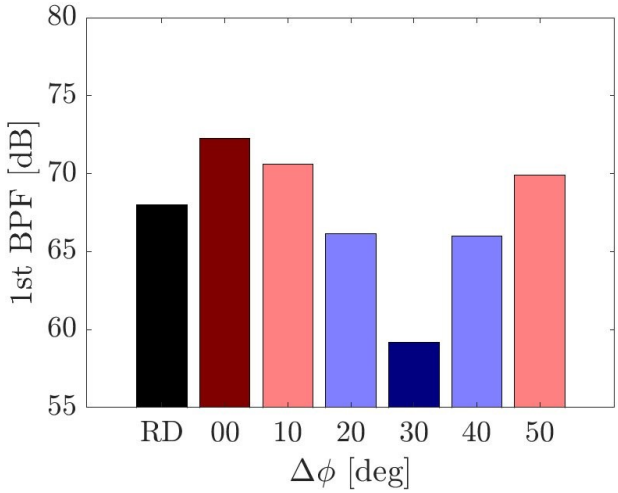


Fig. 15 First BPF sound in the 90° direction from the experimental study for the different values of $\Delta\phi$. [30]

and $\Delta\phi = 15°$ cases is relatively steady over different radiation angles. This is also observed when looking at the difference in OASPL that is recorded experimentally, with the case of $\Delta\phi = 20°$ presented as an example in Fig. 16.

VIII. Conclusions and lesson learned

In these lecture notes we summarized the numerical and experimental studies that were presented as part of the ENODISE Lecture Series. The main take-home message is that both numerical and experimental methods possess unique properties and strengths, and an optimal study of systems requires to leverage the benefits of both. More specifically, we believe that a combination of numerical and experimental studies does not require identical results between the two, which is something that is often sought in validation studies. Perfectly matching results with these two techniques requires extreme measures to be taken for both, e.g., on the numerical side resolving all physical features of all sizes to correctly capture them with the correct magnitude, and on the experimental side omitting every form of background noise that pollutes experimental results in directions with limited noise radiation. Additionally, both

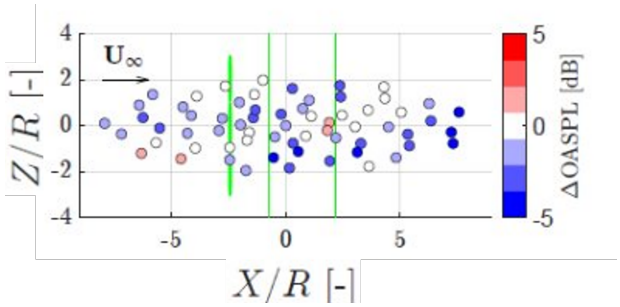


Fig. 16 Difference in the OASPL at the different microphones in the experimental study for $\Delta\phi = 20°$. [30]

experimental and numerical techniques have their own considerations in the setup of the study. The experimental study with the adjacent propellers contained a wing, which directly serves as a mounting body for the hubs. Numerically, however, the wing would have required to resolve a boundary layer on a large surface and a fine enough mesh to propagate the relevant acoustic and hydrodynamic structures all the way towards this surface, which would have substantially increased the computational cost. Instead of aiming for an exact match between both methods (which requires to deal with the weaknesses of both), we therefore believe that there is much more benefit in comparing observations of specific phenomena and verifying trends, as this enables the utilization of the strengths of both approaches.

This project has received funding from the European Union's Horizon 2020 research and innovation programme under grant agreement No 860103.

References

[1] European Commission and Directorate-General for Mobility and Transport and Directorate-General for Research and Innovation, Flightpath 2050: Europe's vision for aviation: maintaining global leadership and serving society's needs, Publications Office, 2011. https://doi.org/doi/10.2777/50266.

[2] NASA, "Strategic Implementation Plan: 2017 Update," https://www.nasa.gov/sites/default/files/atoms/files/sip-2017-03-23-17-high.pdf, Washington, DC, 2017.

[3] Borer, N. K., Patterson, M. D., Viken, J. K., Moore, M. D., Bevirt, J., Stoll, A. M., and Gibson, A. R., "Design and Performance of the NASA SCEPTOR Distributed Electric Propulsion Flight Demonstrator," 16th AIAA Aviation Technology, Integration, and Operations Conference, American Institute of Aeronautics and Astronautics, 2016. https://doi.org/10.2514/6.2016-3920, URL https://arc.aiaa.org/doi/10.2514/6.2016-3920.

[4] Stoll, A. M., Stilson, E. V., Bevirt, J., and Pei, P. P., "Conceptual Design of the Joby S2 Electric VTOL PAV," 14th AIAA Aviation Technology, Integration, and Operations Conference, American Institute of Aeronautics and Astronautics, 2014. https://doi.org/10.2514/6.2014-2407, URL https://arc.aiaa.org/doi/10.2514/6.2014-2407.

[5] Alvarez, E. J., and Ning, A., "Modeling Multirotor Aerodynamic Interactions Through the Vortex Particle Method," American Institute of Aeronautics and Astronautics, 2019. https://doi.org/10.2514/6.2019-2827, URL https://arc.aiaa.org/doi/10.2514/6.2019-2827.

[6] Kim, H. D., Perry, A. T., and Ansell, P. J., "A review of distributed electric propulsion concepts for air vehicle technology," 2018 AIAA/IEEE Electric Aircraft Technologies Symposium (EATS), IEEE, 2018, pp. 1–21.

[7] Kummer, J., and Dang, T., "High-Lift Propulsive Airfoil with Integrated Crossflow Fan," Journal of Aircraft, Vol. 43, 2006, pp. 1059–1068. https://doi.org/10.2514/1.17610.

[8] Zhou, W., Ning, Z., Li, H., and Hu, H., "An Experimental Investigation on Rotor-to-Rotor Interactions of Small UAV Propellers," 35th AIAA Applied Aerodynamics Conference, American Institute of Aeronautics and Astronautics, 2017. https://doi.org/10.2514/6.2017-3744.

[9] Alvarez, E., Schenk, A., Critchfield, T., and Ning, A., "Rotor-on-Rotor Aeroacoustic Interactions of Multirotor in Hover," Vol. 4053, Brigham Young University Faculty Publications, 2020, p. 13.

[10] de Vries, R., van Arnhem, N., Sinnige, T., Vos, R., and Veldhuis, L. L., "Aerodynamic interaction between propellers of a distributed-propulsion system in forward flight," Aerospace Science and Technology, Vol. 118, 2021, p. 107009. https://doi.org/10.1016/j.ast.2021.107009, URL https://linkinghub.elsevier.com/retrieve/pii/S1270963821005198.

[11] Lee, H., and Lee, D.-J., "Rotor interactional effects on aerodynamic and noise characteristics of a small multirotor unmanned aerial vehicle," Vol. 32, No. 4, Physics of Fluids, 2020. https://doi.org/10.1063/5.0003992.

[12] Zarri, A., Dell'Erba, W., Edoardo Munters, and Schram, C., "Fuselage scattering effects in a hovering quadcopter drone," 28th AIAA/CEAS Aeroacoustics 2022 Conference, American Institute of Aeronautics and Astronautics, 2022. https://doi.org/10.2514/6.2022-3031, URL https://arc.aiaa.org/doi/10.2514/6.2022-3031.

[13] Roger, M., "On Combined Propeller Synchronization And Edge Scattering For The Noise Reduction Of Distributed Propulsion Systems," 2019, p. 8.

[14] de Prenter, F., Zarri, A., and Casalino, D., "Low-Cost Computational Modeling of Aeroacoustic Interactions between Adjacent Propellers," 30th AIAA/CEAS Aeroacoustics 2024 Conference, American Institute of Aeronautics and Astronautics, 2024. https://doi.org/10.2514/6.2024-3069, URL https://arc.aiaa.org/doi/abs/10.2514/6.2024-3069.

[15] Pascioni, K. A., Rizzi, S. A., and Schiller, N., "Noise Reduction Potential of Phase Control for Distributed Propulsion Vehicles," American Institute of Aeronautics and Astronautics, 2019. https://doi.org/10.2514/6.2019-1069, URL https://arc.aiaa.org/doi/10.2514/6.2019-1069.

[16] Zhou, T., and Fattah, R., "Tonal Noise Acoustic Interaction Characteristics of Multi-Rotor Vehicles," American Institute of Aeronautics and Astronautics, 2017. https://doi.org/10.2514/6.2017-4054, URL https://arc.aiaa.org/doi/10.2514/6.2017-4054.

[17] Chauhan, S. S., and Martins, J. R. R. A., "Tilt-Wing eVTOL Takeoff Trajectory Optimization," Journal of Aircraft, Vol. 57, 2020, pp. 93–112. https://doi.org/10.2514/1.C035476.

[18] Wick, A. T., Hooker, J. R., and Zeune, C. H., "Integrated Aerodynamic Benefits of Distributed Propulsion," 53rd AIAA Aerospace Sciences Meeting, American Institute of Aeronautics and Astronautics, 2015, p. 1500. https://doi.org/10.2514/6.2015-1500.

[19] Lee, T., Ni, T., and Lin, G., "Aerodynamics and Flowfield of Distributed Electric Propulsion Tiltwing During Transition With Deflected Trailing-Edge Flap," Journal of Fluids Engineering, Vol. 146, 2024. https://doi.org/10.1115/1.4063934.

[20] de Vries, R., and Vos, R., "Aerodynamic Performance Benefits of Over-the-Wing Distributed Propulsion for Hybrid-Electric Transport Aircraft," Journal of Aircraft, Vol. 60, 2023, pp. 1201–1218. https://doi.org/10.2514/1.C036909.

[21] Broadbent, E., "Noise shielding for aircraft," Progress in Aerospace Sciences, Vol. 17, 1976, pp. 231–268. https://doi.org/10.1016/0376-0421(76)90009-9.

[22] Müller, L., Heinze, W., Kožulović, D., Hepperle, M., and Radespiel, R., "Aerodynamic Installation Effects of an Over-the-Wing Propeller on a High-Lift Configuration," Journal of Aircraft, Vol. 51, 2014, pp. 249–258. https://doi.org/10.2514/1.C032307.

[23] Perry, A. T., Bretl, T., and Ansell, P. J., "Aeropropulsive Coupling Effects on a General-Aviation Aircraft with Distributed Electric Propulsion," Journal of Aircraft, Vol. 58, 2021, pp. 1351–1363. https://doi.org/10.2514/1.C036048.

[24] Marcus, E. A., de Vries, R., Kulkarni, A. R., and Veldhuis, L. L., "Aerodynamic Investigation of an Over-the-Wing Propeller for Distributed Propulsion," 2018 AIAA Aerospace Sciences Meeting, American Institute of Aeronautics and Astronautics, 2018, p. 2053. https://doi.org/10.2514/6.2018-2053.

[25] Cooper, R., McCann, W. J., and Chapleo, A. Q., "Over wing propeller aerodynamics," ICAS PROCEEDINGS, American Institute of Aeronautics and Astronautics, 1992, pp. 266–266.

[26] Veldhuis, L., "Propeller wing aerodynamic interference," Ph.D. thesis, Delft University of Technology, 2005.

[27] Johnson, J. L., and White, R. E., "Exploratory low-speed wind-tunnel investigation of advanced commuterconfigurations including an over-the-wing propeller design," Aircraft Design, Systems and Technology Meeting, AIAA, 1983, p. 2531.

[28] Dekker, H., Tuinstra, M., Baars, W. J., Scarano, F., and Ragni, D., Aeropropulsive Performance Modelling of Over-The-Wing Propulsion at Incidence, 2023. https://doi.org/10.2514/6.2023-3355, URL https://arc.aiaa.org/doi/abs/10.2514/6.2023-3355.

[29] Dekker, H., Brouwer, H., Kok, J., Laban, M., and Tuinstra, M., Tonal Noise Measurements and Simulations of an Over-The-Wing Propeller, 2023. https://doi.org/10.2514/6.2023-3358, URL https://arc.aiaa.org/doi/abs/10.2514/6.2023-3358.

[30] d. Monteiro, F., Duivenvoorden, R., Ragni, D., Avallone, F., and Sinnige, T., Experimental Analysis of Synchrophasing Impact on Noise of Distributed Propeller Systems in Tractor Configuration, ???? https://doi.org/10.2514/6.2024-3421, URL https://arc.aiaa.org/doi/abs/10.2514/6.2024-3421.

[31] Grande, E., Ragni, D., Avallone, F., and Casalino, D., "Laminar Separation Bubble Noise on a Propeller Operating at Low Reynolds Numbers," AIAA Journal, Vol. 60, 2022, pp. 5324–5335. https://doi.org/https://doi.org/10.2514/6.2018-2952.

[32] Zarri, A., Koutsoukos, A., and Avallone, F., Aerodynamic and Acoustic Interaction Effects of Adjacent Propellers in Forward Flight, ???? https://doi.org/10.2514/6.2023-4489, URL https://arc.aiaa.org/doi/abs/10.2514/6.2023-4489.

[33] Bhatnagar, P. L., Gross, E. P., and Krook, M., "A Model for Collision Processes in Gases. I. Small Amplitude Processes in Charged and Neutral One-Component Systems," Phys. Rev., Vol. 94, 1954, pp. 511–525. https://doi.org/10.1103/PhysRev.94.511, URL https://link.aps.org/doi/10.1103/PhysRev.94.511.

[34] Yakhot, V., and Orszag, S. A., "Renormalization-Group Analysis of Turbulence," Phys. Rev. Lett., Vol. 57, 1986, pp. 1722–1724. https://doi.org/10.1103/PhysRevLett.57.1722, URL https://link.aps.org/doi/10.1103/PhysRevLett.57.1722.

[35] Romani, G., and Casalino, D., "Rotorcraft blade-vortex interaction noise prediction using the Lattice-Boltzmann method," Aerospace Science and Technology, Vol. 88, 2019, pp. 147–157. https://doi.org/https://doi.org/10.1016/j.ast.2019.03.029, URL https://www.sciencedirect.com/science/article/pii/S1270963818321011.

[36] Farassat, F., "Derivation of Formulations 1 and 1A of Farassat," 2007.

[37] Casalino, D., "An advanced time approach for acoustic analogy predictions," J. Sound Vib., Vol. 261, 2003, pp. 583–612. https://doi.org/10.1016/S0022-460X(02)00986-0.

[38] Avallone, F., Casalino, D., and Ragni, D., "Impingement of a propeller-slipstream on a leading edge with a flow-permeable insert: A computational aeroacoustic study," Vol. 17, No. 6, 2018, pp. 687–711. https://doi.org/10.1177/1475472X18788961, URL http://journals.sagepub.com/doi/10.1177/1475472X18788961.

[39] Romani, G., Grande, E., Avallone, F., Ragni, D., and Casalino, D., "Performance and noise prediction of low-Reynolds number propellers using the Lattice-Boltzmann method," Aerospace Science and Technology, 2021, p. 107086. https://doi.org/https://doi.org/10.1016/j.ast.2021.107086, URL https://www.sciencedirect.com/science/article/pii/S1270963821005964.

[40] Casalino, D., Grande, E., Romani, G., Ragni, D., and Avallone, F., "Definition of a benchmark for low Reynolds number propeller aeroacoustics," Aerospace Science and Technology, Vol. 113, 2021, p. 106707. https://doi.org/https://doi.org/10.1016/j.ast.2021.106707, URL https://www.sciencedirect.com/science/article/pii/S1270963821002170.

[41] Casalino, D., Barbarino, M., and Visingardi, A., "Simulation of Helicopter Community Noise in Complex Urban Geometry," AIAA Journal, Vol. 48, No. 8, 2011, pp. 1614–1624.

[42] Goldstein, M. E., Aeroacoustics, 1976.